Video Article

Growth and Electrostatic/chemical Properties of Metal/$LaAlO_3$/$SrTiO_3$ Heterostructures

Diogo Castro Vaz[1], Edouard Lesne[1,2], Anke Sander[1], Hiroshi Naganuma[1,3], Eric Jacquet[1], Jacobo Santamaria[1,4], Agnès Barthélémy[1], Manuel Bibes[1]

[1]Unité Mixte de Physique CNRS/Thales, Université Paris-Saclay

[2]Max Planck Institut für Mikrostrukturphysik

[3]Department of Applied Physics, Tohoku University

[4]Instituto de Magnetismo Aplicado, Universidad Complutense de Madrid

Correspondence to: Diogo Castro Vaz at diogo.vaz@cnrs-thales.fr

URL: https://www.jove.com/video/56951
DOI: doi:10.3791/56951

Keywords: Engineering, Issue 132, 2D electron gas, oxide interfaces, $LaAlO_3$, $SrTiO_3$, magnetotransport, X-ray photoelectron spectroscopy, pulsed laser deposition, sputtering

Date Published: 2/8/2018

Citation: Vaz, D.C., Lesne, E., Sander, A., Naganuma, H., Jacquet, E., Santamaria, J., Barthélémy, A., Bibes, M. Growth and Electrostatic/chemical Properties of Metal/$LaAlO_3$/$SrTiO_3$ Heterostructures. *J. Vis. Exp.* (132), e56951, doi:10.3791/56951 (2018).

Abstract

The quasi 2D electron system (q2DES) that forms at the interface between $LaAlO_3$ (LAO) and $SrTiO_3$ (STO) has attracted much attention from the oxide electronics community. One of its hallmark features is the existence of a critical LAO thickness of 4 unit-cells (uc) for interfacial conductivity to emerge. Although electrostatic mechanisms have been proposed in the past to describe the existence of this critical thickness, the importance of chemical defects has been recently accentuated. Here, we describe the growth of metal/LAO/STO heterostructures in an ultra-high vacuum (UHV) cluster system combining pulsed laser deposition (to grow the LAO), magnetron sputtering (to grow the metal) and X-ray photoelectron spectroscopy (XPS). We study step by step the formation and evolution of the q2DES and the chemical interactions that occur between the metal and the LAO/STO. Additionally, magnetotransport experiments elucidate on the transport and electronic properties of the q2DES. This systematic work not only demonstrates a way to study the electrostatic and chemical interplay between the q2DES and its environment, but also unlocks the possibility to couple multifunctional capping layers with the rich physics observed in two-dimensional electron systems, allowing the fabrication of new types of devices.

Video Link

The video component of this article can be found at https://www.jove.com/video/56951/

Introduction

Quasi 2D electron systems (q2DES) have been extensively used as a playground to study a multitude of low-dimensional and quantum phenomena. Starting from the seminal paper on the $LaAlO_3$/$SrTiO_3$ system (LAO/STO)[1], a burst of different systems that host new interfacial electronic phases have been created. Combining different materials led to the discovery of q2DESs with additional properties, such as electric-field tunable spin polarization[2], extremely high electron mobilities[3] or ferroelectricity-coupled phenomena[4]. Although an immense body of work has been dedicated to unravel the creation and manipulation of these systems, several experiments and techniques have shown contradictory results, even in rather similar conditions. Additionally, the balance between electrostatic and chemical interactions was found to be essential to correctly understand the physics at play[5,6,7].

In this article, we thoroughly describe the growth of different metal/LAO/STO heterostructures, using a combination of pulsed laser deposition (PLD) and *in situ* magnetron sputtering. Then, to understand the effect of different surface conditions in the buried q2DES at the LAO/STO interface, an electronic and chemical study is performed, using transport and electron spectroscopy experiments.

Since multiple methods have been previously used to grow crystalline LAO on STO, the choice of appropriate deposition techniques is a crucial step for the fabrication of high quality oxide heterostructures (in addition to possible cost and time constrains). In PLD, an intense and short laser pulse hits the target of the desired material, which is then ablated and gets deposited on the substrate as a thin film. One of the major advantages of this technique is the ability to reliably transfer the stoichiometry of the target to the film, a key element in order to achieve the desired phase formation. Furthermore, the capability of performing layer-by-layer growth (monitored in real time using reflection high-energy electron diffraction - RHEED) of a vast number of complex oxides, the possibility of having multiple targets inside the chamber at the same time (allowing the growth of different materials without breaking vacuum) and the simplicity of the setup make this technique one of the most effective and versatile.

Yet, other techniques such as molecular beam epitaxy (MBE) allow the growth of even higher quality epitaxial growth. Instead of having a target of a specific material, in MBE each specific element is sublimed towards the substrate, where they react with each other to form well defined

Copyright © 2018 Journal of Visualized Experiments

atomic layers. Additionally, the absence of highly energetic species and more uniform energy distribution allows the fabrication of extremely sharp interfaces[8]. This technique is however much more complex than PLD when it comes to the growth of oxides, since it must be performed in ultra-high vacuum conditions (so that the long mean free path is not destroyed) and requires in general a larger investment, cost- and time-wise. Although the growth process used in the first LAO/STO publications was PLD, samples with similar characteristics have been grown by MBE[9]. It is also worth noting that LAO/STO heterostructures have been grown using sputtering[10]. Although atomically sharp interfaces were achieved at high temperatures (920 °C) and high oxygen pressures (0.8 mbar), interfacial conductivity was not achieved.

For the growth of the metallic capping layers, we use magnetron sputtering, as it provides a good balance between quality and flexibility. Other chemical vapor deposition based techniques might however be used to achieve similar results.

Lastly, the combination of transport and spectroscopy techniques showed in this article exemplifies a systematic way of probing both electronic and chemical interactions, emphasizing the importance of crosschecking different approaches to fully understand the many features of these types of systems.

Protocol

Note: All 5 steps described in this protocol can be paused and restarted at any time, with the single condition that the sample is kept under high vacuum from step 3.4 through 5.

1. STO(001) Substrate Termination:

1. Fill an ultrasonic cleaner (with a 40 kHz transducer) with water and heat it to 60 °C. Fill a borosilicate glass beaker with acetone. Independent of the beaker size, be sure to fill it with at least 20% of its maximum volume, to ensure that the substrates are well submerged.
    1. Place an out of the box mix-terminated single-side polished (001)-oriented STO single-crystal substrate (55 mm^2 in lateral size, 0.5 mm in thickness, miscut angle between 0.01° and 0.02°) inside the borosilicate glass beaker.
    2. Sonicate the substrate in acetone for 3 min. Dry the substrate using a nitrogen blow gun with an operating pressure of about 5 bar.
2. Repeat the procedure of step 1.1 but using isopropanol and then deionized water.
3. Place the clean substrate in a sample holder made of polyvinylidene fluoride, PVDF, with a "dipper" shape (**Figure 1a**). Fill a second borosilicate glass beaker (**Figure 1b**) with running deionized water.
   Note: The beaker should be big enough so that the sample holder fits in it.
4. Place the substrate in the sample holder.
5. Wearing appropriate protection, fill a beaker (**Figure 1b**), typically made of Polytetrafluoroethylene, PTFE, to about 20% of its maximum volume, with a buffered hydrofluoric (HF) solution ($HF:NH_4F$ = 1:7). Use approximately the same size beaker as the one used in step 1.3.
6. Submerge the sample holder in HF for exactly 30 s and immediately move it into the deionized running water to stop any subsequent chemical reactions. Agitate it lightly.
7. After 2 min, remove the sample holder from the deionized water. Take out the substrate and dry it with a nitrogen blow gun.
   Note: More details can be found within Kawasaki's recipe[11].
   Caution: The HF solution used is highly corrosive and poisonous. Always carry out the manipulation and disposal of used HF solutions in appropriate working environments. Symptoms of poisoning after contact with a body part might start to be visible up to one day after exposure and may not cause any pain in the first few hours. It is also possible to use an alternative termination process based on a HCl-HNO_3 acidic solution[12] or an acid-free termination recipe[13].
8. Insert the substrate in a tube furnace (**Figure 1c**) at 20 °C. Set the furnace partial pressure to approximately 1 atm of oxygen. Ramp the temperature to 1000 °C at a rate of 20 °C/min. Anneal the substrates for 3 hours at 1000 °C. After the 3 hours, let the sample cool down to 20 °C. Remove the substrate. Close the oxygen source.
9. Repeat step 1.1 to remove subsequent surface contaminations promoted during annealing.

2. Preparation of the single-crystal LAO target:

1. Mechanically polish a single-crystal LAO target (1-inch diameter) gently using sandpaper and isopropanol solution as a lubricant. Dry it using a nitrogen blow gun.
2. Mount the target in a carousel.
   Note: Be sure that the carousel allows target rotation.
3. Insert the carousel in the loadlock chamber (**Figure 2**). Let the target degas in vacuum, while continuously pumping the chamber (until it reaches a pressure in the 10^{-8} mbar range). Transfer the carousel to the PLD chamber (**Figure 3a** and **3b**). Wait until the base pressure is in the 10^{-9} mbar range.
   Note: In the absence of a loadlock chamber and *in vacuo* transfer system, the typical waiting time and base pressure can be severely affected.
4. Inspect the laser energy using an excimer laser energy meter. To do this, use a rectangular slit (6 mm x 16 mm) and an external attenuator right after the laser source to modulate the shape and energy of the beam (**Figure 4a** and **4b**). Place the energy meter in the path of the laser beam, between the second converging lens and the quartz window. Then, shoot the laser at an arbitrary frequency and read the energy using the energy meter.
5. Set the energy to be the same (or marginally higher) as the one used during the growth (step 3.12).
   Note: Absolute values of the laser energy might vary depending on the geometry of the setup. However, for LAO target ablation, use a laser fluence of about 1 J/cm^2 (fluence = energy/spot area). Also, use a pulsed KrF excimer laser of wavelength λ=248 nm, with a characteristic pulse duration of 25 ns and operated at a minimum of 21 kV (for improved pulse-to-pulse reproducibility).
6. Rotate the LAO target at about 10 rpm (using the rotation platform of the carrousel, where the target is mounted).

1. Adapt the target rotation speed to the spot size and laser repetition rate to avoid two consecutive overlapping shots, potentially leading to some local overheating or melting of the target and subsequent off-stoichiometry. A visual description is provided in **Figure 4c**.

7. Insert oxygen in the chamber until an oxygen partial pressure of $2x10^{-4}$ mbar is achieved. Remove the energy meter. Pre-ablate the LAO target at 3 or 4 Hz for 20000 pulses.
   Note: The laser should be set up so that the angle between the beam and the target is 45° (**Figure 4d**). This relatively long ablation of the LAO single-target was found to have a determinant role in LAO/STO sample-to-sample reproducibility.

3. PLD growth:

1. Perform an atomic force microscopy (AFM) scan of the previously terminated STO substrate surface to verify termination, morphology and cleanness (**Figure 5**).
2. Using silver paste, glue the substrate, with the terminated surface pointing upwards, to a sample holder. Although the orientation of the substrate is not relevant, be sure that it is placed in the center of the holder (**Figure 6a**).
3. Heat it up to about 100 °C for 10 min so that the solvent evaporates and the paste solidifies (for optimum thermal conduction). Let the sample holder cool down.
4. Insert the sample holder inside the loadlock. Using the arm within the cluster, transfer the sample holder to the XPS chamber to analyze the oxygen, carbon and titanium peaks (refer to step 5 for more details).
5. Transfer the sample holder to the PLD chamber, with the substrate facing down towards the LAO target (**Figure 6b**).
6. Insert oxygen inside the chamber to reach an oxygen partial pressure of $2x10^{-4}$ mbar. Raise the temperature of the sample holder to 730 °C (at 25 °C/min).
7. Using reflective high energy electron diffraction (RHEED), align the electron beam at grazing angle (between 1° and 3°) with the substrate surface so that the diffraction spots are observed on the phosphor screen. Monitor in real-time the intensity of each spot using a CCD camera and image analysis software. Use a source voltage of 30 kV and current of 40 µA.
8. Place the sample holder 63 mm away from the target.
   Note: The target-to-substrate distance might require some degree of optimization depending on the geometry of the PLD setup used.
9. Shoot the laser in order to calibrate the energy so that it matches about 1 J/cm^2 (in the same fashion as in step 2.4). Again, use a rectangular slit (6 mm x 16 mm) and an external attenuator right after the laser exit to modulate the shape and energy of the beam (**Figure 4a** and **4b**).
10. Set the laser frequency to 1 Hz. Stop shooting the laser and remove the energy meter.
11. Start the rotation of the LAO target (same way as in step 2.6). Initiate the RHEED oscillations reading. Wait until it stabilizes.
12. Start shooting the laser. Observe the plume (**Figure 6c**) and the RHEED oscillations (**Figure 6d**). Stop the laser at the peak of one of the oscillation depending on the desired thickness.
    Note: Remember that each oscillation represents one unit cell (uc) grown. For the purpose of this experiment, grow 1 and 2 uc for transport and spectroscopic experiments, respectively.
13. After the growth is finished, shutdown the RHEED gun and proceed to the post-annealing step.
    Note: The post-annealing step is done right after the growth is finished.
    1. To start the post-annealing, increase the oxygen partial pressure in the chamber from $2x10^{-4}$ mbar (growth pressure) to $1x10^{-1}$ mbar and decrease the temperature of the sample holder from 730 °C (growth temperature) to 500 °C.
    2. After the temperature and pressure are stabilized, introduce a static oxygen partial pressure of about 300 mbar, while keeping the sample holder temperature at 500 °C. Leave the sample in these conditions for 60 min.
14. Cool down the sample at 25 °C/min while keeping it in the same oxygen partial pressure until it reaches room temperature.
15. Transfer the sample to the XPS chamber to investigate possible valence changes in the titanium peak or the relative La/Al concentration (refer to step 5 for more details).
16. To ensure that the LAO surface is kept pristine, transfer the sample *in vacuo* to the sputtering chamber (**Figure 7a**), which is kept at all times at a pressure in the range of 10^{-8} mbar.
    Note: Performing these experiments *ex situ* will cause the accumulation of carbon and water on the surface which ultimately leads to altered results.

4. Magnetron Sputtering of Metallic Overlayers:

Note: Depending on the desired metal, parameters such as Ar pressures, deposition currents and target-to-substrate distances might vary slightly. It is advised to optimize each deposition process depending on the geometry of the sputtering setup used. The following procedure describes the deposition of 3 nm of Co.

1. Place the sample with the surface facing down towards the target.
2. Insert pure Ar inside the sputtering chamber to achieve an atmosphere of about $4.5x10^{-4}$ mbar (about 100 sccm).
3. Position the substrate (LAO/STO) about 7 cm away from the Co target.
4. With the shutter closed, ramp the current up to about 100 mA (36 W) so that the plasma is ignited.
5. With a stable plasma (**Figure 7b**), lower the current to 80 mA (deposition current) as well as the inflow of Ar to 5.2 sccm. Ensure that the plasma stays stable.
6. Pre-sputter the Co target for about 5 min to remove any oxidized layer that may have formed at its surface.
7. With the sample at room temperature, open the shutter and deposit for 25 s. Close the shutter to conclude the deposition.
   1. For transport experiments, deposit a subsequent capping layer of about 3 nm of Al (whose surface passivates, forming an AlOx protective layer upon exposure to air) to prevent oxidation of the underlying metallic layer.
      Note: The growth rate is not measured directly inside the chamber. In order to do this, grow various samples with different deposition times while using the same parameters. Then, measure the thickness of each sample using X-ray reflectometry. Do this procedure once for each metallic target used.

8. Ramp the current down to zero, close the Ar source and pump the chamber.
9. Transfer once more the sample holder to the XPS chamber (**Figure 8a**) to inspect possible valence change at the Ti 2p level as well as a possible oxidation at the metal/LAO interface (refer to step 5 for more information).

5. In Situ X-ray Photoelectron Spectroscopy:

1. Place the sample with the surface normal aligned parallel to the electron analyzer axis (**Figure 8b**).
2. Approach the X-ray gun as close as possible to the sample (avoid mechanical contact between the end of the gun and the sample holder to prevent damage) and turn it on.
    1. In this experiment, use an Mg Kα source with an excitation energy of 1253.6 eV. Set the filament to achieve an emission current of 20 mA at an anode voltage of 15 kV. Regarding the analyzer electron-optics, choose an entrance slit of 2 mm of diameter and an exit slit with rectangular shape of 5x11 mm.
    Note: Refer to the manual of the XPS setup used for information regarding maximum emission currents and anode voltages. Also, the size of entrance and exit slips might be different for other specific setups. If the analyzer has different specifications, choose the slits in a way to avoid too high intensity in the electron counting unit.
3. After turning the X-ray gun on, ensure that the chamber is in ultra-high vacuum conditions (10^{-10} mbar range). Collect the survey spectra (between 0 and 1200 eV binding energy) with a selected step of 0.05 eV, a dwell time of 0.5 s, a pass energy between 30 and 60 eV and an adequate lens mode to achieve the smallest spot size possible. Adjust the values depending on the resolution intended.
    1. Locate the position of the relevant peaks (**Figure 8c**). For improved statistics, measure each peak several times and average the spectra collected.
4. Analyze the spectra using adequate XPS processing software.
    1. In order to identify the electrons from a given transition, define an energy range that comprises the peak to analyze.
    2. Create an appropriate background curve (normally a Shirley background[14]) and subtract it from the original data.
    3. Using bibliographic references[15], locate the possible peaks that compose the measured peak. Pay special attention to tabulated distances and relative intensities for different peaks.
    Note: A more in depth look at the XPS data collected is provided in the "Representative Results" section as well as in Ref.[7].

6. Magnetotransport Experiments:

1. Using an ultrasonic wedge-bonding machine, wire-bond the metal/LAO/STO sample with Al or Au wires to contact the buried interface (**Figure 9a**).
Note: Select an appropriate wedge-to-sample distance, force and time, depending on the setup used and the type of transport measurement holder.
2. Use an 8-wire geometry (4 in van der Pauw -channel 1- and 4 in Hall geometry -channel 2-). To do this, start by contacting one of the channels of the transport measurement holder to the four corners of the sample in van der Pauw geometry. Then, contact a second channel to the contacts previously done in the sample (**Figure 9b**).
3. Check if contacts are good by measuring the resistance with a multimeter. To ensure that the sample is uniform, verify that the resistance measured in different directions is roughly the same, so that the van der Pauw $R_{100} \approx R_{010}$ condition is satisfied.
Note: If R_{100} and R_{010} are significantly different, the van der Pauw measurement should be performed in both directions (following Ref.[16]). Previous studies report strong anisotropic electric transport properties in LAO/STO[17].
4. Mount the holder in a transport setup.
    1. Measure the resistance (channel 1) down to 2 K.
    2. At low temperature, measure sequentially the magnetoresistance (channel 1) and Hall effect (channel 2) by sweeping an external and perpendicular magnetic field (from -9 to 9 T), sourcing a current of typically 10 to 100 μA for metal/LAO/STO samples.
    3. Repeat step 6.4.2. for 5 K, 10 K, 50 K, 100 K, 200 K and 300 K, in order to observe the magnetoresistance evolution with temperature.

Representative Results

The full experimental system used for growth and characterization is shown in **Figure 2**. Having different setups connected in UHV through a distribution chamber is highly recommended to ensure that the surface of the sample after each growth process is kept pristine. The PLD chamber (**Figure 3**), magnetron sputtering (**Figure 7**) and XPS chamber (**Figure 8**) are also described in detail. Additional information regarding the optical path in the PLD setup is displayed in **Figure 4a** and **4b** (adapted from Ref.[18]). We note that the conditions discussed in the protocol for each technique may vary depending on the exact geometry of each chamber, type of targets used or the type of equipment.

We confirmed atomically flat and clean STO surfaces, before starting the growth, through atomic force microscopy (AFM), as seen in **Figure 5a**. A "step and terrace" like structure with single unit cell step height is evidenced due to the miscut angle in respect to the (001) plane orientation. All samples were grown on substrates with a step size of about 250 nm (for a miscut angle between 0.01 and 0.02°) and a step height between 2.5 and 5 nm. Both LAO and metal films reproduce the surface morphology of the layers beneath, as seen in **Figure 5b**.

During PLD growth, a plume is generated through the process of ablating species from the target towards the substrate, as shown in **Figure 6c**. For an oxygen partial pressure of $2x10^{-4}$ mbar, the plume has a light purple color and is not very bright. Note that the intensity and color of the plume depend heavily on the oxygen pressure, fluence and type of target material used. Altering the fluence was previously shown to modify the La/Al cationic ratio, which might ultimately lead to a modulation of the interfacial conducting properties[19,20]. Also, RHEED monitoring is used to ensure layer-by-layer growth. Typical RHEED data is shown in **Figure 6d** for a 2 uc growth of LAO on STO.

An XPS analysis of the bare STO substrate allows us to confirm the virtual absence of additional features in the oxygen peak, usually present due to attached water and hydrogen molecules (**Figure 8d**), as well as a very small amount of adsorbed carbon. The heating process used during the PLD growth normally removes/reduces these features. An analysis performed on a LAO/STO sample reveals the appearance of La and Al peaks and an additional intensity decrease of Ti and Sr peaks, due to the attenuation introduced by the LAO film. Note that the Al peaks are hardly observable from a survey scan, since only 1 uc of LAO was deposited. Finally, an XPS analysis performed after metal deposition shows clear attenuation of all peaks coming from the LAO/STO. As we discuss ahead, analysis of the peaks associated with the deposited metal gives us information regarding its oxidation state. All survey spectra addressed are displayed in **Figure 8c**.

Transport experiments are performed at low temperature (2K) using an 8-wire geometry (4 wires for transverse measurements and 4 wires for Hall measurements), as shown in **Figure 9a** and **9b**. Measurements show strikingly different behavior depending on the metallic capping layer chosen. LAO(2 uc)/STO samples capped with noble metals such as Au, Pt or Pd showed a linear Hall trace with a change in resistance of a few tens of mΩ over 9 T (**Figure 9c**). However, similar samples capped with reactive metals such as Ti, Ta, Co, $Ni_{80}Fe_{20}$ and Nb (2.5 nm) showed signatures of a 2DES, namely S-shaped Hall traces (**Figure 9d**). We conclude that from a transport point of view, LAO/STO samples below the 4 uc critical thickness (that in regular conditions are insulating) form an interfacial q2DES if a reactive metal is added on top. Capping with noble metals leads to an insulating interface, where only the metal layer is detected (see **Figure 9c** and inset of **Figure 9d**). Indeed, these results are consistent with theoretical prediction performed on similar heterostructures[21]. They also seem to support that for metals with lower work functions (φ) electron transfer towards the STO is favored, which explains why for Au capped samples there is no 2DES detected but for Co and Ta capped the carrier density is approximately $3x10^{13}$ and $4x10^{13}$ cm^{-2} (note that $\Phi_{Ta} < \Phi_{Co} < \Phi_{Au}$) A more in depth analysis of this transport data may be found in the methods sections of Ref.[7].

Although, an electrostatic approach seems to fully describe this system, chemical reactions must be considered[22,23,24]. By depositing a highly reactive metal such as Ta on LAO/STO, oxygen tends to diffuse towards the metal so that it starts to oxidize. From an XPS point of view (**Figure 10a**), two things are seen: first, various Ta oxide peaks appear (**Figure 10b**) and the metallic Ta feature is partially (or totally) suppressed; second, due to outward oxygen diffusion, oxygen vacancies form at the surface of the perovskite, so that electrons are released to the lattice. Ti atoms in the STO are then able to host some of these electrons therefore forming a q2DES. Consequently, the valence state of Ti changes from 4+ to 3+ which gives rise to an additional feature on the lower binding energy side of the Ti peak (see **Figure 10c** and **10d**). The analysis of this Ti^{3+} feature might then be correlated with the number of carriers in the q2DES[25].

Angle-dependent studies can also provide valuable information on the depth profile. If the electron takeoff angle is 90° (surface normal parallel with the electron analyzer axis) then the maximum volume is probed. When the takeoff angle decreases (tilted sample) electrons from the same depth will travel larger distances, so that the total volume measured is reduced. An angle-dependent study is shown on the inset of **Figure 10d**. Note that by changing the angle from 0° to 50° roughly the same Ti^{3+} intensity is observed, meaning that the q2DES region extends more that the XPS maximum probing depth (of about 5nm). These results clearly show the importance of backing transport experiments with electron spectroscopy and vice versa. For more details on the analysis refer to Ref.[7].

Copyright © 2018 Journal of Visualized Experiments

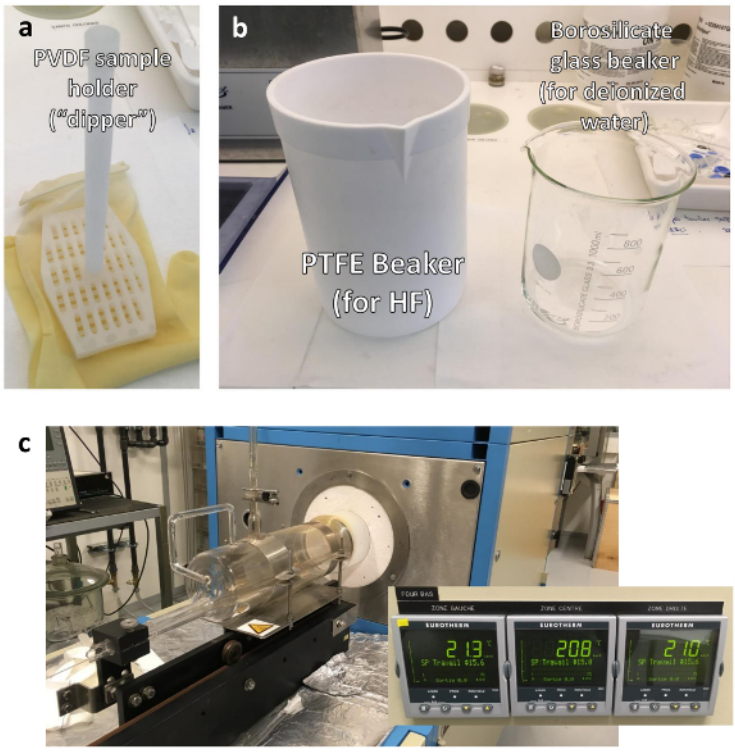

Figure 1: Materials used for STO substrate termination. (a) PTFE beaker for HF and borosilicate glass beaker for deionized water. **(b)** PVDF sample holder with "dipper" shape. Notice that both beakers should be large enough so that the dipper fits inside them. **(c)** Tube furnace used to anneal the substrates after termination. Three thermostats control the temperature in three different positions of the furnace. Please click here to view a larger version of this figure.

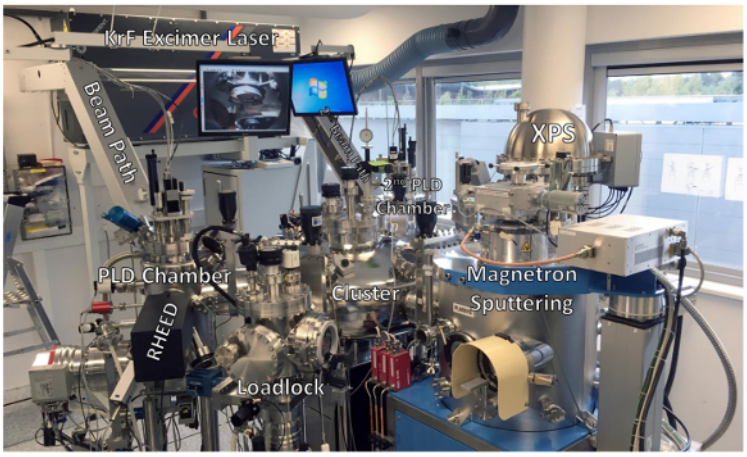

Figure 2: Complete setup. All setups, including the pulsed laser deposition chamber, magnetron sputtering and X-ray photoelectron spectroscopy, are connected through a cluster that allows for sample transfer without breaking vacuum (10^{-9} mbar range). A sample is initially inserted in the loadlock and the valve that connects it to the cluster is open. An arm located inside the cluster is then able to pick up the sample and move it to any of the setups mentioned. Please click here to view a larger version of this figure.

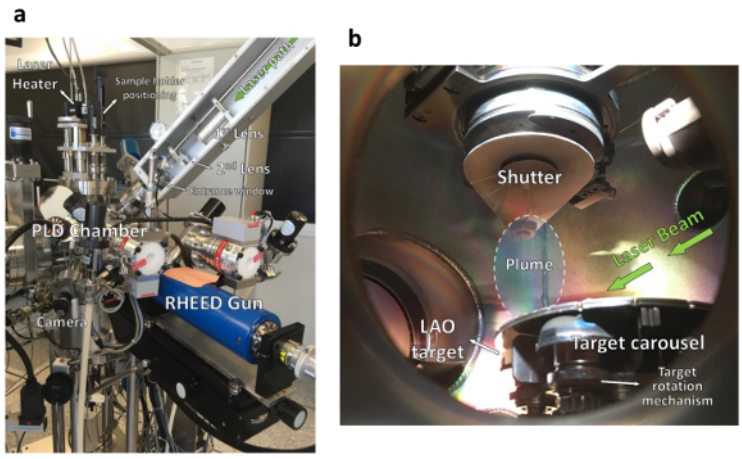

Figure 3: Pulsed laser deposition system. (a) Exterior of the PLD chamber. Although not visible, the phosphor screen and camera used to monitor the RHEED diffracted electrons are behind the chamber, aligned with the RHEED gun. **(b)** Interior of the PLD chamber. The target carousel allows the storage of 5 different targets inside the chamber at the same time. Please click here to view a larger version of this figure.

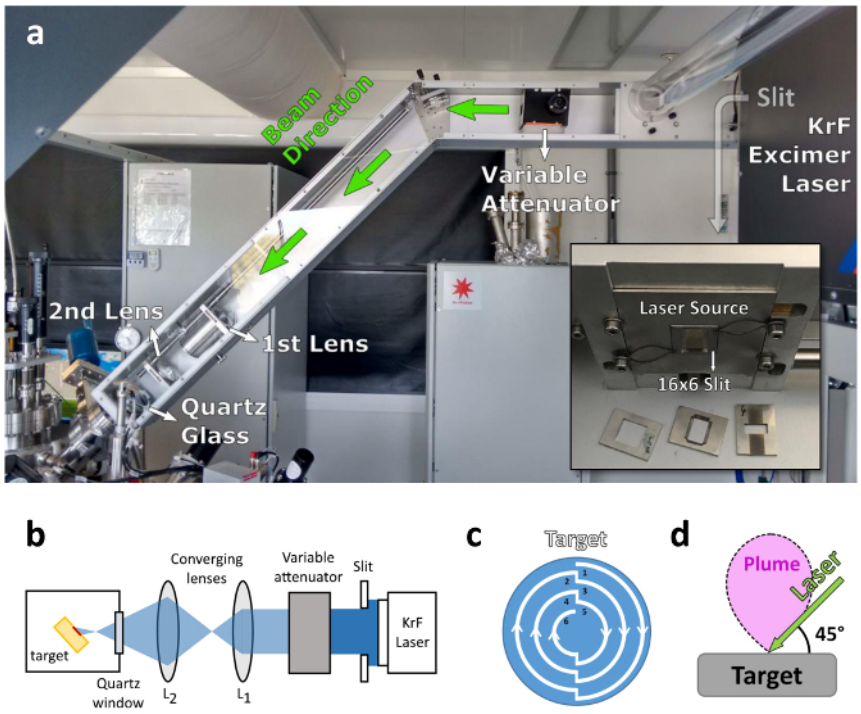

Figure 4: Optics for the PLD system. (a) The beam exits the laser and is immediately reduced in size through a slit. The variable attenuator allows the control of the beam energy without varying the source laser parameters. Two converging lenses are then used to focus the beam on the target. **(b)** Detailed sketch of the optical apparatus (modified from Ref.[18]). **(c)** To avoid two subsequent shots on the same place, which might overheat the target, the target rotation is programmed so that it follows the pattern showed. The laser starts by ablating the outermost curve (path number 1). After doing half a rotation (90°) it continues to ablate along path number 2. After another 90° it moves to path number 3, and so on. At the end of path number 6 it goes back to path number 1. **(d)** The laser ablation, performed at 45°, generates a plume that expands perpendicularly to the target. Please click here to view a larger version of this figure.

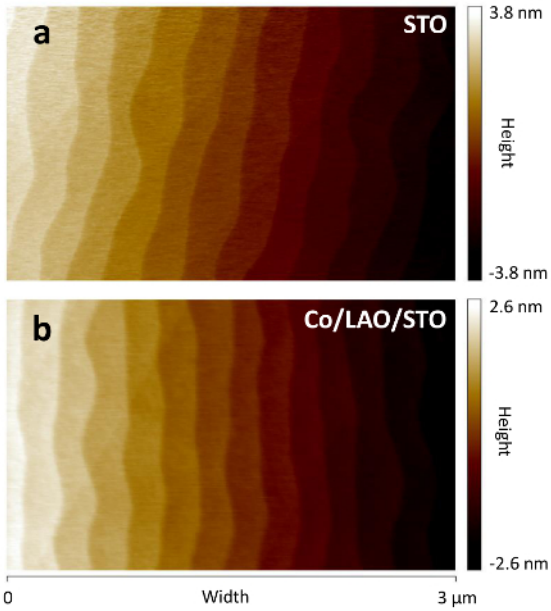

Figure 5: Atomic force microscopy of (a) a STO substrate used for the growth of **(b)** a Co(2nm)/LAO(2 uc)/STO sample. Please click here to view a larger version of this figure.

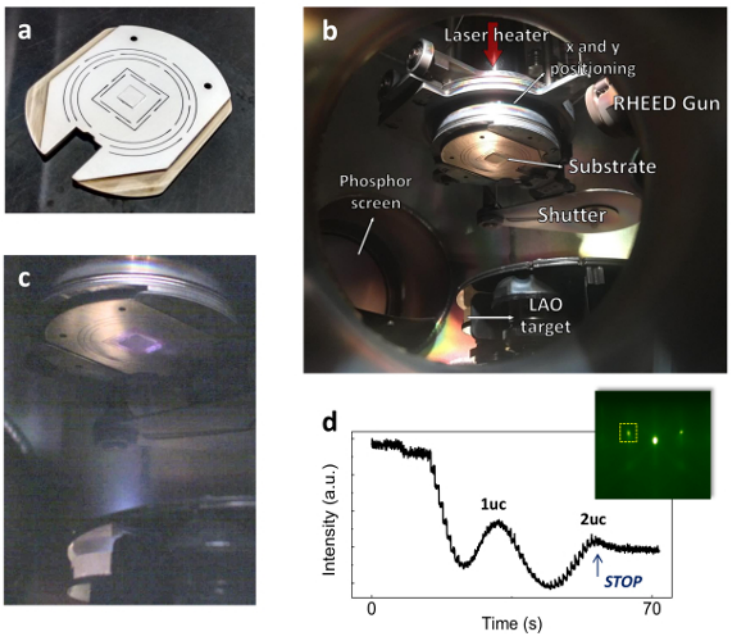

Figure 6: Growth of LAO ultra-thin films (a) STO substrate mounted on a substrate holder with silver paste. **(b)** Interior of the PLD chamber. An infrared laser is used to locally heat the back-side of the sample holder. x and y positioning are controlled through knobs on the outside of the chamber. **(c)** Characteristic plume formed after ablating the LAO target with a single beam pulse, at $2x10^{-4}$ mbar of oxygen. **(d)** Typical RHEED oscillations and diffraction spots. For consistency, monitoring is always performed on the (0-1) diffraction spot, located inside the yellow dotted box. Please click here to view a larger version of this figure.

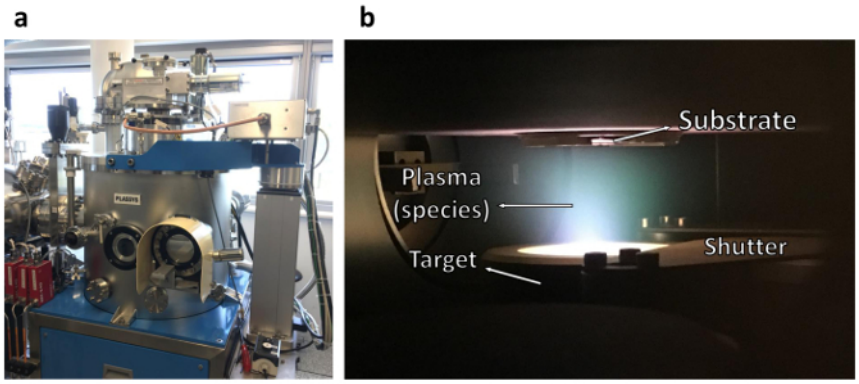

Figure 7: Magnetron sputtering system. (a) Exterior of the sputtering chamber. **(b)** Interior of the sputtering chamber. Ar atoms are accelerated towards the metal target, located inside the shown cylinder and mounted on a dc-magnetron source, hence generating a plasma. Please click here to view a larger version of this figure.

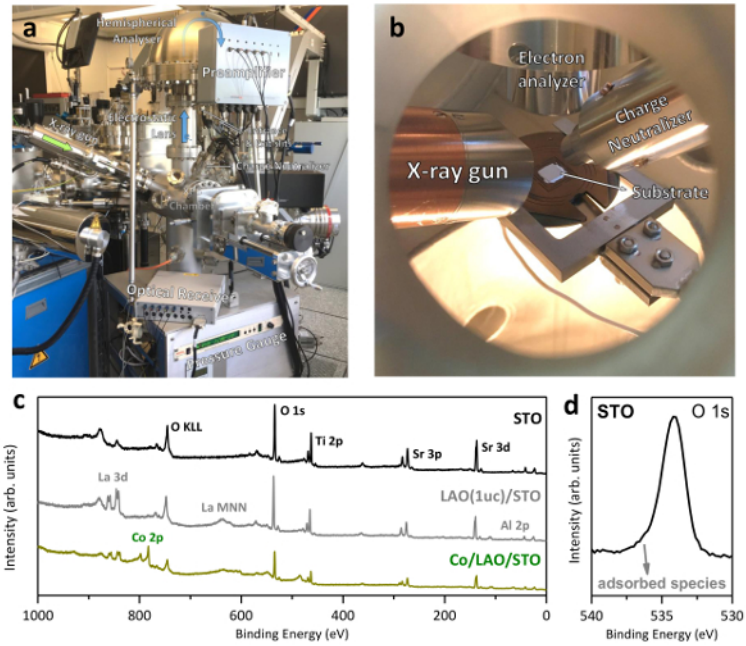

Figure 8: X-ray photoelectron spectroscopy system. (a) Exterior of the XPS chamber. Emitted electrons enter the transfer lens of the analyzer. There, they are retarded/accelerated to match the analyzer pass energy before entering the analyzer itself and being finally collected by the electron detector. A preamplified signal is then sent to the optical receiver before reaching the amplifier and computer. **(b)** Interior of the XPS chamber. The X-ray gun can be retracted to allow positioning of the sample holder. **(c)** Typical survey scan performed on a bare STO substrate, an LAO(1 uc)/STO and a Co/LAO(1 uc)/STO. Note the evolution of the peaks. Ti and Sr peaks are gradually attenuated as the top layer thickness increases. La and barely visible Al peaks appear after LAO growth. The addition of an ultra-thin layer (3 Å) of Co rapidly attenuates all the other peaks. **(d)** Zoomed O 1s peak (STO substrate). Note that a very small tail is observed at the high binding energy side of the peak, signaling slight adsorption of water and carbon molecules. Please click here to view a larger version of this figure.

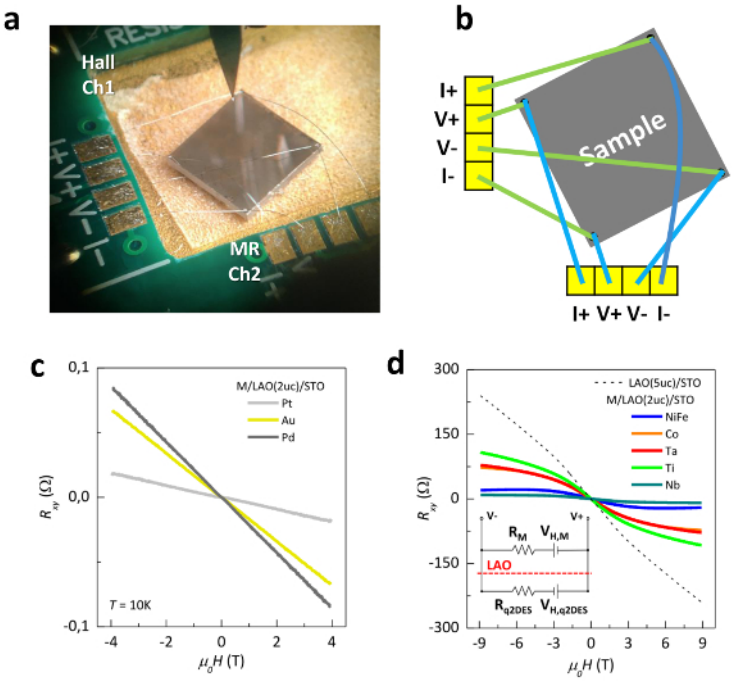

Figure 9: Transport properties of metal/LAO/STO heterostructures. (a) Wire bonding of a sample in a **(b)** 8-wire geometry (4-wire for Hall resistance and 4-wire for longitudinal resistance) sketch. This geometry allows the collection of both Hall and magnetoresistance, sequentially sourcing between the two channels, yet in a single measurement run. Hall resistance R_{xy} as a function of applied perpendicular magnetic field $\mu_0 H$ of LAO(2 uc)/STO samples capped with **(c)** noble metals and **(d)** reactive metals. The inset shows a schematic circuit after wire bonding, where R_M and R_{q2DES} represent the longitudinal resistances and $V_{H,M}$ and $V_{H,q2DES}$ the Hall voltages generated in each layer. This figure has been modified from D.C. Vaz *et al.*[7]. Please click here to view a larger version of this figure.

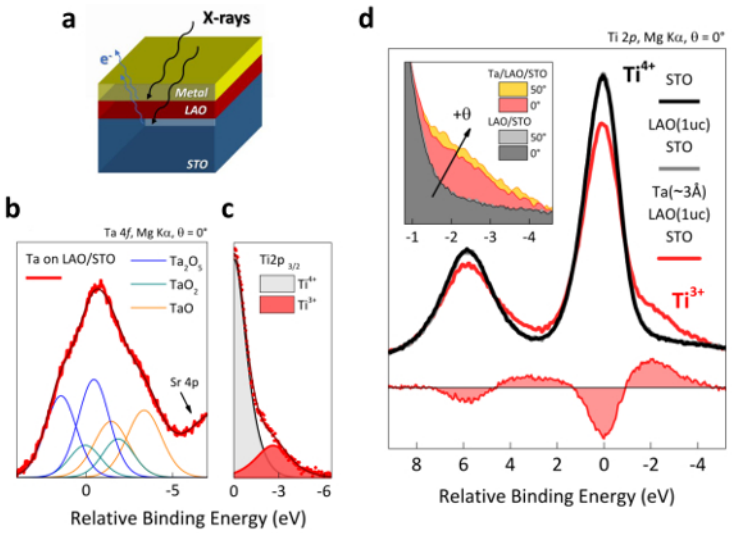

Figure 10: X-ray photoelectron spectroscopy of Ta/LAO/STO heterostructures. (a) Schematic sketch of the measurement performed. Photoelectrons emitted by X-ray excitation carry information on both the LAO/STO and the metal/LAO interface. **(b)** The Ta 4f spectra informs on the oxidation level of the metallic capping used. The spectra can be fitted exclusively with different Ta oxide peaks, indicating that 100% of the metal layer has oxidized on top of the oxide heterostructure. **(c)** Fitting the Ti 2p peak with two components, 4+ and 3+, allows us to extract a Ti^{3+}/Ti^{4+} intensity ratio of 20%. **(d)** Spectra collected on Ta/LAO/STO samples (in red) at the Ti 2p level show an additional (Ti^{3+}) shoulder at lower binding energy, associated with extra electrons hosted at the interfacial Ti atoms. Additionally, the inset shows the weak angle-dependence of the Ti^{3+} feature, revealing that the extension of the q2DES formed at the LAO/STO interface is larger than the maximum electron probing depth. This figure has been modified from D.C. Vaz *et al.*[7]. Please click here to view a larger version of this figure.

Discussion

During substrate termination, one should be extremely careful with the submerging time in HF solution. We observed under- and over-etched surfaces by varying just 5 s with regard to the original recipe. Additionally, we observed a dependence between substrate step size and submerging time. For smaller step sizes (less than 100 nm) submerging 30 s might lead to over-etching, even though afterwards the annealing procedure might be sufficient to properly reconstruct the surface. Due to the risks of using HF based acids, we also advise the optimization of an HCl-HNO_3 acidic solution termination[12] or an acid-free termination technique[13] which should lead to similar results.

Concerning the growth of LAO, we advise the use of single crystal targets to avoid the possible preferential ablation of specific species, which might occur for example in ceramic/sintered targets. In our case, samples grown with a ceramic target resulted in insulating samples, most likely due to off stoichiometry of the grown films[20]. The 20000 pulses pre-ablation step we describe might seem overly long, however we observed that the transport properties deteriorate extremely quickly by overlooking this step. Pre-ablating with less than 10000 pulses repeatedly showed insulating LAO/STO interfaces. As expected from PLD growth we additionally advise not to grow on substrates larger than 10 mm x 10 mm in lateral size. 4-point electrical probing on different regions of these 10x10 samples showed slight inconsistencies likely due to off-stoichiometry issues at the samples corners. We also note that all samples were grown with the center of the plume vertically aligned with the substrate. At low oxygen pressure (lower than 10^{-2} mbar) and due to the low target-substrate distance, ablated species travel in a ballistic regime, which might also justify why the fluence utilized affects so drastically the properties of the interfacial conductivity[19].

Since the laser energy measurement is done outside the chamber and the laser entrance window gets coated over time, which yields to a loss of transmission, we guide ourselves by targeting a constant growth rate value instead. After about 15 growths, the window can differ up to 20 mJ from the energy measured outside. The optimized growth rate for LAO was found to be approximately 25 pulses/unit cell for our specific PLD growth process, equivalent to an (outside) energy of about 60 mJ.

The RHEED oscillations measured during growth are extremely sensitive to the fine positioning of the substrate. The exact same growth process might result in substantial differences in terms of RHEED oscillations intensities. We advise using the same positioning parameters and probing the same diffraction spots for every growth. We have grown all of our samples monitoring only the (01) diffraction spot, since this will mostly show the elastic scattering events that the electrons undergo at the crystal surface, while the (00) spot might carry some additional undesired background information on inelastic scattering events[26]. TEM imaging showed good uniformity and confirmed, together with standard X-ray diffraction, the correct corresponding number of LAO unit cells.

Finally, as mentioned in the introduction, the fabrication of LAO/STO structures has been successfully achieved by either PLD or MBE. Both techniques require a high level of optimization, however, we recommend the following: MBE should be used when the interface quality is critical for the experiment, as it provides high quality heterostructures with a great control of layer thickness and very low defect concentration[8]. Yet, it possesses slower deposition rates and involves a larger investment.

PLD on the other hand also provides the means to create high quality samples. It has the benefits of being versatile (allowing multiple targets inside the chamber at the same time), cost-efficient, fast (growth may last less than 2 min) and conceptually simple. Since it is based on the ablation of high energy species against a substrate it might however lead to a slightly bigger concentration of defects. As an example, a comparative study of $LaNiO_3$/$LaAlO_3$ heterostructures grown by PLD and MBE is shown in Ref.[27]. Note also that while MBE has been implemented before for large scale deposition of different materials, PLD is now also being considered as a possible candidate for industrial applications[28].

Concerning the sputtering deposition, we emphasize that different metals have different wetting behaviors on top of oxide substrates[22]. Consider increasing the thickness accordingly to achieve full coverage. Films under a few nm in thickness might result in non-percolated films. Perform SEM characterization after deposition to verify good uniformity.

Using slower deposition rates and less energetic incoming species is also recommended, to finely control the film's thickness and avoid possible penetration of sputtered species into the sample. To do this, one might increase the target-substrate distance and/or reduce the plasma excitation current.

Regarding the XPS measurements, since the measurements are performed *in situ*, there is no electrical connection between the metallic overlayer (or the q2DES) and the sample holder. This means that charging effects will be severe due to the insulating nature of the STO substrate. We therefore advise not to conclude on the position of the collected peaks, since they might be shifted several eV. It is also known that metals tend to screen electrons quite efficiently so that a 1 nm metallic capping might already impede probing other buried layers. Additional charge compensation by a flood gun might help to avoid peak shifting and deformation. In our case, peak deformation was negligible since we used a non-monochromatic X-ray source providing enough secondary electrons.

Angle-dependent studies can also provide valuable information on the depth profile. If the electron takeoff angle is 90° (surface normal parallel with the electron analyzer axis) then the maximum volume is probed. When the takeoff angle decreases (tilted sample) electrons from the same depth will travel larger distances, so that the total volume measured is reduced. One is then able to, for example, assess the thickness of a q2DES through a valence state depth-dependent analysis, as was previously shown for LAO/STO heterostructures[25].

We also bring the attention to additional peaks seen in the survey spectra. If the sample size is smaller than the detected area of the electron analyzer, traces of silver paste on the borders of the sample and of the species deposited on the substrate holder, such as La or Al, are collected. Note that these species will, to some extent, suffer different charging effects, which will lead for example to the appearance of double peak features. This can be easily fixed by reducing the entrance slit size for electron collection and increase the dwell time (for higher electron count).

Overall, although the instructions provided in this paper serve as a guide to grow LAO ultra-thin films, they demonstrate a generic way of growing most ABO_3 perovskites with PLD. Even though each material will require specific steps for optimized desired structural, electrical, or magnetic

Copyright © 2018 Journal of Visualized Experiments

properties, one should be especially attentive to some essential features: type and composition of the target[29], oxygen partial pressures during growth and annealing[30,31], substrate temperature, ablation frequency and laser fluence[19,32] and type of substrates (and previous surface treatments).

Through a combination of transport and spectroscopy experiments, we are also able to draw a more accurate and complete picture of a complex system where capturing the interplay between electrostatic and chemical phenomena is essential to understand the intrinsic versus extrinsic doping mechanisms. We reiterate that due to their strongly correlated character, these complex oxide systems are extremely sensitive to small stoichiometry and electronic changes such that their comprehensive study requires different complementary *in situ* and *ex situ* techniques.

Disclosures

The authors have nothing to disclose.

Acknowledgements

This work received support from the ERC Consolidator Grant #615759 "MINT", the region Île-de-France DIM "Oxymore" (project "NEIMO") and the ANR project "NOMILOPS". H.N. was partly supported by the EPSRC-JSPS Core-to-Core Program, JSPS Grant-in-Aid for Scientific Research (B) (#15H03548). A.S. was supported by the Deutsche Forschungsgemeinschaft (HO 53461-1; postdoctoral fellowship to A.S.). D.C.V. thanks the French Ministry of Higher Education and Research and CNRS for financing of his PhD thesis. J.S. thanks the University Paris-Saclay (D'Alembert program) and CNRS for financing his stay at CNRS/Thales.

References

1. Ohtomo, A., Hwang, H. Y. A high-mobility electron gas at the $LaAlO_3/SrTiO_3$ heterointerface. *Nature.* **427**, 423-426 (2004).
2. Stornaiuolo, D. *et al.* Tunable spin polarization and superconductivity in engineered oxide interfaces. *Nat. Mater.* **15** (3), 278-283 (2015).
3. Chen, Y. Z. *et al.* Extreme mobility enhancement of two-dimensional electron gases at oxide interfaces by charge-transfer-induced modulation doping. *Nat. Mater.* **14** (8), 801-806 (2015).
4. Rödel, T.C. *et al.* Universal Fabrication of 2D Electron Systems in Functional Oxides. *Adv. Mater.* **28** (10), 1976-1980 (2016).
5. Xie, Y., Hikita, Y., Bell, C., Hwang, H. Y. Control of electronic conduction at an oxide heterointerface using surface polar adsorbates. *Nat. Commun.* **2**, 494 (2011).
6. Scheiderer, P., Pfaff, F., Gabel, J., Kamp, M., Sing, M., Claessen, R. Surface-interface coupling in an oxide heterostructure: Impact of adsorbates on $LaAlO_3/SrTiO_3$. *Phys. Rev. B.* **92** (19) (2015).
7. Vaz, D. C. *et al.* Tuning Up or Down the Critical Thickness in $LaAlO_3/SrTiO_3$ through In Situ Deposition of Metal Overlayers. *Adv. Mater.* **29** (28), 1700486 (2017).
8. Schlom, D. G. Perspective: Oxide molecular-beam epitaxy rocks! *APL Mater.* **3** (6), 1-6 (2015).
9. Segal, Y., Ngai, J. H., Reiner, J. W., Walker, F. J., Ahn, C. H. X-ray photoemission studies of the metal-insulator transition in $LaAlO_3/SrTiO_3$ structures grown by molecular beam epitaxy. *Phys. Rev. B.* **80** (24), 241107 (2009).
10. Dildar, I. M. *et al.* Growing $LaAlO_3/SrTiO_3$ interfaces by sputter deposition. *AIP Adv.* **5** (6), 67156 (2015).
11. Kawasaki, M. *et al.* Atomic control of the $SrTiO_3$ crystal surface. *Science (80-.).* **266**, 1540 (1994).
12. Zhang, J. *et al.* Depth-resolved subsurface defects in chemically etched $SrTiO_3$. *Appl. Phys. Lett.* **94** (9), 1-4 (2009).
13. Connell, J. G., Isaac, B. J., Ekanayake, G. B., Strachan, D. R., Seo, S. S. A. Preparation of atomically flat $SrTiO_3$ surfaces using a deionized-water leaching and thermal annealing procedure. *Appl. Phys. Lett.* **101** (25), 98-101 (2012).
14. Heide, P. Van Der *X-ray Photoelectron Spectroscopy: An introduction to Principles and Practices.* **2011** (2011).
15. Wagner, C. D., Riggs, W. M., Davis, L. E., Moulder, J. F. *Handbook of X-ray Photoelectron Spectroscopy.* John Wiley & Sons, Inc: Eden Prairie, Minnesota, USA (1979).
16. Pauw, L. J. A method of measuring the resistivity and Hall coefficient on lamellae of arbitrary shape. *Philips Tech. Rev.* **20**, 220-224 (1958).
17. Brinks, P., Siemons, W., Kleibeuker, J. E., Koster, G., Rijnders, G., Huijben, M. Anisotropic electrical transport properties of a two-dimensional electron gas at $SrTiO_3$-$LaAlO_3$ interfaces. *Appl. Phys. Lett.* **98** (24), 242904 (2011).
18. Lesne, E. Non-Equilibrium Spin Accumulation Phenomenon at the $LaAlO_3/SrTiO_3$(001) Quasi-Two-Dimensional Electron System, *Ph.D. Thesis.* Université Pierre et Marie Curie, France. (2015).
19. Sato, H. K., Bell, C., Hikita, Y., Hwang, H. Y. Stoichiometry control of the electronic properties of the $LaAlO_3/SrTiO_3$ heterointerface. *Appl. Phys. Lett.* **102** (25), 251602 (2013).
20. Warusawithana, M. P. *et al.* $LaAlO_3$ stoichiometry is key to electron liquid formation at $LaAlO_3/SrTiO_3$ interfaces. *Nat. Commun.* **4** (2013).
21. Arras, R., Ruiz, V. G., Pickett, W. E., Pentcheva, R. Tuning the two-dimensional electron gas at the $LaAlO_3/SrTiO_3$(001) interface by metallic contacts. *Phys. Rev. B.* **85** (12) (2012).
22. Fu, Q., Wagner, T. Interaction of nanostructured metal overlayers with oxide surfaces. *Surf. Sci. Rep.* **62** (11), 431-498 (2007).
23. Chen, Y. *et al.* Metallic and Insulating Interfaces of Amorphous $SrTiO_3$-based Oxide Heterostructures. *Nano Lett.* **11** (9), 3774-3778 (2011).
24. Posadas, A. B. *et al.* Scavenging of oxygen from SrTiO3 during oxide thin film deposition and the formation of interfacial 2DEGs. *J. Appl. Phys.* **121** (10) (2017).
25. Sing, M. *et al.* Profiling the interface electron gas of $LaAlO_3/SrTiO_3$ heterostructures with hard x-ray photoelectron spectroscopy. *Phys. Rev. Lett.* **102** (17) (2009).
26. Hasegawa, S. Reflection High-Energy Electron Diffraction. *Charact. Mater.* (October 2012), 1925-1938 (2012).
27. Wrobel, F. *et al.* Comparative study of $LaNiO_3/LaAlO_3$ heterostructures grown by pulsed laser deposition and oxide molecular beam epitaxy. *Appl. Phys. Lett.* **110** (4), 0-5 (2017).
28. Blank, D. H. A., Dekkers, M., Rijnders, G. Pulsed laser deposition in Twente: from research tool towards industrial deposition. *J. Phys. D. Appl. Phys.* **47** (3), 34006 (2014).

Copyright © 2018 Journal of Visualized Experiments

29. Preziosi, D., Sander, A., Barthélémy, A., Bibes, M. Reproducibility and off-stoichiometry issues in nickelate thin films grown by pulsed laser deposition. *AIP Adv.* **7** (1) (2017).
30. Hensling, F. V. E., Xu, C., Gunkel, F., Dittmann, R. Unraveling the enhanced Oxygen Vacancy Formation in Complex Oxides during Annealing and Growth. *Sci. Rep.* **7**, 39953 (2017).
31. Xu, C., Bäumer, C., Heinen, R. A., Hoffmann-Eifert, S., Gunkel, F., Dittmann, R. Disentanglement of growth dynamic and thermodynamic effects in $LaAlO_3/SrTiO_3$ heterostructures. *Sci. Rep.* **6**, 22410 (2016).
32. Breckenfeld, E. *et al.* Effect of growth induced (non)stoichiometry on interfacial conductance in $LaAlO_3/SrTiO_3$. *Phys. Rev. Lett.* **110** (19) (2013).

Copyright © 2018 Journal of Visualized Experiments